Basics of Additive Manufacturing Processes for High-Entropy Alloys

A Zavdoveev, T Baudin, D G Mohan, D Pakula, D Vedel, M Skoryk

BASICS OF ADDITIVE MANUFACTURING PROCESSES FOR HIGH ENTROPY ALLOYS

ОСНОВИ АДИТИВНОГО ВИРОБНИЦТВА ВИСОКОЕНТРОПІЙНИХ СПЛАВІВ

A. Zavdoveev[1], T. Baudin[2], D. G. Mohan[3], D. Pakula[4], D. Vedel[5], M. Skoryk[4]

[1]Paton Electric Welding Institute of NAS of Ukraine,
Bozhenko n. 11, 03680 Kiev, Ukraine,
[2]Université Paris-Saclay, CNRS, Institut de chimie moléculaire et des matériaux d'Orsay, 91405 Orsay, France,
[3]Department of Material Processing Engineering, Zhengzhou Research Institute of Harbin Institute of Technology, Zhengzhou, China,
[4]G. V. Kurdyumov Institute of Metal Physics of the NAS of Ukraine;
Kyiv, Ukraine
[5]I.M. Frantsevich Institute of Problems of Materials Science NAS of Ukraine,
st. Krzyzanowski, 303142, Kyiv, Ukraine

This review offers a comprehensive analysis of additive manufacturing (AM) processes in the application of High Entropy Alloys (HEAs). HEAs have gained considerable attention in recent years due to their unique mechanical and physical properties. It is provided historical background and a clear definition of HEAs, outlining their development over time. The focus concentrated on examining the utilization of AM processes in HEAs. Specifically, three prominent AM techniques are discussed: Electron Beam Processes, Laser-Processed HEAs, and Wire Arc Additive Manufacturing. Each technique is explored in detail, including its advantages, limitations, and current applications within the HEAs field.

Subsequently, the delves into the significance of AM process parameters when fabricating HEAs. Parameters such as laser power, scanning speed, and powder feed rate are analyzed for their effects on the microstructure and mechanical properties of the final product. Lastly, it addresses post-processing techniques for additive-manufactured HEAs. It emphasizes the importance of steps such as heat treatment, surface finishing, and machining in achieving desired material properties and dimensional accuracy in AM-produced HEA components. By presenting a comprehensive overview of HEAs, their application in AM processes, the influence of process parameters, and post-processing considerations, this review paper serves as a valuable resource for researchers and practitioners seeking to advance the understanding and implementation of AM in the HEAs domain.

Цей огляд пропонує комплексний аналіз процесів адитивного виробництва (АВ) у застосуванні до високоентропійних сплавів (ВЕС). В останні роки ВЕС привернули значну увагу завдяки своїм унікальним механічним і фізичним властивостям. Надається історична довідка та чітке визначення ВЕС з описом їх розвитку з часом. Основна увага зосереджена на вивченні використання процесів АВ у ВЕС. Зокрема, обговорюються три відомі методи АВ: електронно-променеві процеси, лазерно-оброблені ВЕС та дугове адитивне виробництво. Кожен метод детально досліджується, включаючи його переваги, обмеження та поточні застосування в галузі ВЕС. Згодом заглиблюється в важливість параметрів процесу АВ під час виготовлення ВЕС. Такі параметри, як потужність лазера, швидкість сканування та швидкість подачі порошку, аналізуються на їх вплив на мікроструктуру та механічні властивості кінцевого продукту. Нарешті, у ньому розглядаються методи пост-обробки для ВЕС, виготовлених за допомогою добавок. Він підкреслює важливість таких етапів, як термічна обробка, фінішна обробка поверхні та механічна обробка для досягнення бажаних властивостей матеріалу та точності розмірів у компонентах ВЕС, виготовлених АВ. Представляючи вичерпний огляд ВЕС, їх застосування в процесах АВ, вплив параметрів процесу та міркування щодо постобробки, цей оглядовий документ служить цінним ресурсом для дослідників і практиків, які прагнуть покращити розуміння та впровадження АВ у домені ВЕС.

Keywords: additive manufacturing, high entropy alloys, processing, structure, properties.

Ключові слова: адитивне виробництво, високоентропійні сплави, обробка, структура, властивості.

1. History and definition of HEAs

Fascinating development of the alloy design brings us principally new materials with superior properties - high entropy alloys (HEAs). The history of creation is alloying principles, which firstly was based on one main element, or two, and other alloying elements in small amounts. A heightened presence of certain ele-

ments, for instance, Fe in Al alloys, can potentially result in a destructive impact[1]. But the things were drastically inverse, since 2004, when the multicomponent approach has given birth to HEAs. Yeh [2] and Cantor [3] have proposed the new paradigm of alloy creation. This paradigm is based on the multicomponent main alloying system, normally more than 5 main elements. Yea et al. However, more recently, researchers have expanded the concept of HEAs to include alloys with three or four principal elements as well [4][5] have presented a new approach to alloy design with multiple principal elements in equimolar or near-equimolar ratios. Despite general knowledge on physical metallurgy that predicted the formation of the multiple intermetallic compounds when using multi principal elements, the real alloys appear much more usable and uniform. The configurational entropy changes per mole, based on Boltzmann's hypothesis, ΔSconf, during the formation of a solid solution from n elements with equimolar fractions may be calculated from the following equation[2].

$\Delta S_{conf} = —k \text{ Ln } w = —R (1/n \text{ Ln } 1/n + 1/n \text{ Ln } 1/n + \cdots 1/n \text{ Ln } 1/n) = —R \text{ Ln } 1/n = R \text{ Ln } n$ (1)

where k is Boltzmann's constant, w is the number of ways of mixing, and R is the gas constant: 8.314 J/K mole. Thus, Yeh et al. [1] have shown, ΔSconf for equimolar alloys with 3, 5, 6, 9, and 13 elements equal to 1.10R, 1.61R, 1.79R, 2.20R, and 2.57R, respectively. In addition, if the formation enthalpies of two strong intermetallic compounds, such as NiAl and TiAl were divided by their respective melting points, the resulting ΔS_{conf}, 1.38R, and 2.06R, are in the same range as the entropy changes of mixing in a system with more than five elements [1]. This evidences that it will be preferable the tendency of ordering while the mechanism of segregation would be suppressed by the high mixing entropy [6].

Thus, alloys with a higher number of principal elements will more preferably forms solid solutions during solidification, instead of intermetallic compounds, except for oxides, carbides, nitrides, and silicides with very large heats of formation [ref].

Yeh et al. have defined high-entropy alloys (HE alloys) as those composed of five (starting from three according to updates) or more principal elements in equimolar ratios or HE alloys may contain principal elements with the concentration of each element being between 35 and 5 at.-%. This has led to many alloy systems with simple crystal structures and extraordinary properties [7].

It is established that HEAs form different microstructures such as single-phase FCC, BCC, HCP microstructures [8][9][10] as well as complex multi-phase microstructures [11]. These alloys have attracted great research interest owing to promising properties observed in specific HEAs. For instance, the quinary equimolar Cantor HEA CrMnFeCoNi possesses an exceptional fracture toughness of more than 200 MPa m1/2 at cryogenic temperatures, making it an ideal material

for low-temperature applications [3]. As usual, HEAs are processed by powder metallurgy [12], conventional casting [8][13], etc. To achieve the needed properties through refining the microstructures, the as-cast HEAs are processed by cold metal forming and/or annealing [8][13]. The traditional metallurgical processes mentioned above are used to create simple geometry parts, with the requirement of post processing. Furthermore, there is a dilemma in the strength-plasticity relation for HEAs. Namely, some HEAs are very strong but restricted with plasticity (BCC non-equi-atomic AlCoCrFeNiTi0.5 [14]), while there are very ductile but not strong enough (quinary equi-atomic CrMnFeCoNi [15]). Cantor et al. have reported [3] several HEAs with a five-component equi-atomic HEA CrMnFeCoNi (Cantor alloy) and a series of six-, seven-, eight- and nine-component equi-atomic HEAs. It is considered [3], a HEA consisting of 20 elements in equiatomic proportions, 5 at.% each of Mg, Sb, Si, Ge, Zn, Bi, Pb, Sn, Cd, Al, Nb, Mo, W, Ag, Cu, Ni, Co, Fe, Cr and Mn. However, HEAs are not restricted to equiatomic ratios. As mentioned above, Yeh et al. [2] expanded the scope of HEAs to alloys with multiple principal elements and concentration of each element between 5 and 35 at.%. There is appearance of non-equiatomic HEAs (e.g. Al0.5CoCrCuFeNi) [13] and four-component HEAs (e.g. NbMoTaW) [16]. Some HEAs with trace elements have been also reported. For instance, Park et al. [17] investigated a novel Cantor alloy with 1 at.% C additions, marked as 1%C-CrMnFeCoNi HEA. Therefore, in this point, HEAs reflect the alloys consisting of multiple elements, each in valuable atomic fractions (from 5 to 35 at.%), possibly with trace alloying elements. It should be underlined that there are ternary equiatomic HEAs (i.e. CrCoNi) in some literature named as medium entropy alloys (MEAs) [18][19]. Unique compositional characteristics and large configurational entropy value of HEAs lead to severe lattice distortion (Fig. 1) due to the differences in atomic size, bonding energy, and crystal structure.

The HEAs as a rule exhibit a single-phase face-centered cubic (FCC), body- centered cubic (BCC) or hexagonal close packing (HCP) solid solution microstructure. For instance, the quinary equiatomic Cantor HEA CrMnFeCoNi crystallizes as a single-phase FCC solid solution structure [8][21]. Moreover, a number of equiatomic quaternary (CrCoNiMn), ternaries (CrCoNi, FeNiMn, NiCoMn) also have a single-phase FCC solid solution structure [5][22][18]. Quaternary non-equiatomic HEA Fe40Mn40Co10Cr10 exhibits a single-phase FCC solid solution structure in as-cast, hot-rolled and homogenized states as reported by Deng et al. [23]. Such microstructure formation was observed in other HEAs (FeNiCrCuMo)[24]. The HEAs containing refractory BCC metals such as W, Mo, Nb, Ta, and V typically crystallize as a single-phase BCC solid solution structure in contrast to the FCC HEAs. Namely, HEAs NbMoTaW and VNbMoTaW exhibit a single-phase BCC solid solution structure as reported by Senkov et al. [16]. Single-

phase BCC solid solution microstructures were also registered for TaNbHfZrTi [25], MoNbHfZrTi [26], as well as for TaNbHfZr [27]. Notably that the metals Ti, Zr, and Hf have an HCP structure at room temperature, changing to a BCC structure at high temperatures revealing allotropic transformation. For a while HEAs with a single-phase HCP solid solution structure are rare, and typically contain several HCP metals such as Y, Ru, Re, Gd, Tb, Dy, Tm, etc. (ex. YGdTbDyLu, GdTbDyTmLu and CoFeReRu)[9][28].

Additionally, to single-phase FCC, BCC or HCP solid solution microstructures, multi- phase microstructures consisting of multiple solid solution phases were also registered in some HEAs. Li et al. [29] have shown that the quaternary non-equiatomic HEA Fe50Mn30Co10Cr10 acquires a dual-phase FCC plus HCP solid solution microstructure due to partial martensitic transformation after quenching from the single-phase FCC region. Fig. 2 shows the as-quenched microstructure that consists of a 72% FCC matrix with ~ 45 μm grain size plus 28% HCP layers from several nanometers to 10 μm in thickness. The typical HEAs are presented in Table 1.

There are complex deformation mechanisms in HEAs: dislocation motion, nano-twinning, or martensitic phase transformation. Concerning these deformation mechanisms, FCC Cantor HEA CrMnFeCoNi [21][31] was the most investigated. For example, the formation and evolution of the deformation substructures in CrMnFeCoNi during tensile straining have been studied [31]. The tensile deformation process is dominated by dislocation motion at low strain levels. With further strain levels increasing up to ~ 7.4% for 77 K and ~ 25% for 293 K, nano-twinning is activated and plays an additional deformation mechanism. The strain hardening capability is increased through the nano-twinning behavior that introduces more interfaces. Fig. 3 shows the formation and hence evolution of the deformation substructures in CrMnFeCoNi during tensile straining at 77 K. Instead of the tensile test while compression, a larger strain value may be needed to activate the nano-twinning mode, since mechanical twinning is still minor when CrMnFeCoNi is compressed to 46% strain [32].

High entropy alloys are manufactured through a range of techniques, which are chosen based on the desired properties, alloy composition, and specific application needs. The prevailing fabrication methods for HEAs include casting, powder metallurgy, and additive manufacturing. Casting, although effective, requires substantial energy consumption and necessitates the use of a furnace with an inert atmosphere[33][34]. Powder metallurgy, while viable, is labor-intensive[35]. Consequently, additive manufacturing emerges as an appealing alternative due to its potential for optimizing the trade-off between fabrication time and energy consumption in the context of HEAs.

2. Overview of AM processes in HEAs application

The AM process produces samples, layer by layer, from a digital design, which increases design and manufacturing freedom. Complex elements can be fabricated in a single step by the AM process, requiring little or no post-machining. The AM process is a localized melting and solidification process that has high solidification velocity and a significant temperature gradient. Moreover, it is possible to achieve hierarchical microstructures characterized by the presence of fine grains, solidification patterns, and dislocation substructures through the fabrication process contributing to exceptional mechanical properties.[36]. Additionally, in-situ phase decomposition during the AM process can lead to the formation of the desirable microstructures and hence good mechanical properties [37][38]. These advantages are the most important argument for the increasing interest in the fabrication of HEAs through the AM process. There are a number of HEAs processed by various AM processes with different processing parameters: AlxCoCrFeNi [22][39], Co1.5CrFeNi1.5Ti0.5Mo0.1 [40], CrMnFeCoNi [41][42], TiZrNbMoV [9], C-containing CrCoNiFe [43] and compositionally graded HEAs, i.e. AlCoxCr1-xFeNi ($0 \leq x \leq 1$) [44].

The rapid heating, melting followed by rapid resolidification of materials in the scale of the melt pool with subsequent numerous reheating-recooling cycles of the as-solidified region, are characteristic for AM process [45]. This complex thermal process determines the solidified microstructures, phase formation, grain structure and substructure, defects, cracks and pores formation, and thus the mechanical properties. So, investigating this thermal process, mostly the rapid solidification process, is of valuable importance for the AM process.

The first such work was done by Brif et al. in 2015 [22] where they adopted a numerical approach based on the Rosenthal model, to reveal a relationship between the melt penetration depth and a number of printing parameters (for selective laser melting, SLM). The printing parameters to ensure that the layers can be fully melted were identified and successfully fabricated the FeCoNiCr HEA with high strength and ductility. In another work, Sun et al. [46] have found that the FeCoNiCr HEA is addicted to solidification cracking under the SLM process, and predicted that the decreased grain size can effectively decrease the depression pressure and thus suppress the solidification cracking susceptibility. The equilibrium and non-equilibrium solidification processes were simulated [47] with the aim to predict the phase formation and elemental redistribution of HEAs. From the elemental powder blends using the laser metal deposition (LMD) process, CrMnFeCoNi HEA was successfully printed. The CrMnFeCoNi HEA with hierarchical microstructures was also additively manufactured by Zhu et al. [41] with mechanical properties comparable to as-casted counterparts (Fig.4).

It should be emphasized that the tensile properties of the AM-ed HEA CrMnFeCoNi were reported to vary in a wide range for yield strength: 200 – 600 MPa and uniform elongation: 20 – 60% [48,49]. This evidences that different manufacturing parameters lead to varied microstructures, namely grain size. These arguments show that the micrometallurgy of AM process plays a key role in HEAs application.

Thus, the strength-plasticity point of the AM HEAs is still a great problem to be solved. For example, CrMnFeCoNi, obtained with AM is the most investigated HEA up to now. It has been successfully manufactured with a good combination of strength and ductility that compares to those as-casted counterparts [41][49]. Some refractory HEAs with high-strength and low-plasticity have been also fabricated, Moorehead et al. [50] (Mo-Nb-Ta-W, single-phase disordered BCC structures), Dobbelstein et al.[51] (Ti25Zr50Nb0Ta25 to Ti25Zr0Nb50Ta25), Kunce et al. [52] (ZrTiVCrFeNi and TiZrNbMoV). Additionally, the AlCoFeNiSmTiVZr HEA system has been also produced by the SLM process, with the research focused on the corrosion features [53].

For different applications, HEAs, owing to large compositional design space, offer unique possibilities to construct mechanical and functional properties of materials. The base effects of high configurational entropy, lattice distortion, mixing effect, and slow diffusion lead to a specter of attractive physical-mechanical, properties [19,54,55]. HEAs can be considered as potential materials for advanced applications such as nuclear, aerospace, cryogenics etc. [56,57]. Due to specific restrictions it is challenging task to fabricate of HEAs with homogeneous microstructure in complex geometries using traditional approaches. Therefore, AM has been of growing interest in HEAs application.

2.1 Electron Beam Processes

Fabrication of HEAs using selective electron beam melting (SEBM) have been published in several reports [58][59]. Successful fabrication of the equiatomic AlCoCrFeNi HEA using SEBM was reported by Fujieda et al.[58] [ref], Kuwabara et al.[40] [ref], and Shiratori et al. [60]. For SEBM-built HEA nano-lamellar morphology with a mixture of FCC + BCC + B2 phases was registered caused by preheating, while as-cast counterpart showed only a BCC + B2 structure. At the bottom of the sample, FCC density was higher and as formed mostly at grain boundaries possibly due to longer preheating, which leads to phase transformation from the BCC phase to FCC. The amount of B2 was also higher in the bottom part of the sample. In the top part of the SEBM sample, the columnar grain with the orientation of <100> along build direction was observed and, in the bottom, equiaxed grains with random orientation were formed. The smaller grain size of the SEBM process

in comparison with as-casted is explained by a higher cooling rate. Moreover, only in the SEBM sample, due to specific cooling conditions, the cellular microstructure was observed. The elemental distribution of both the SEBM and as-cast alloys reveal fluctuation inside the grains, and the segregation of Co and Fe at the grain boundaries as well as at sub-grain boundaries. A similar microstructure was obtained for CoCrFeMnNi HEA produced using EBM [61]. The hierarchical microstructure with large columnar grains along build direction (strong <100> texture) and cellular dendritic structure for EBM built CoCrFeMnNi HEA was reported by Wang et al. [61]. The equiaxed grains perpendicular to the build direction with intragranular cellular dendritic microstructures were observed. The segregation of Fe, Cr, and Co into the dendrites, and Mn and Ni segregated into the interdendritic regions were found. The needle-like Ni3Ti intermetallic in Co1.5CrFeNi1.5Ti0.5Mo0.1 HEA fabricated using EBM were revealed during microstructure characterization. Phases with basket-weave morphology precipitated homogeneously in the matrix, and were dissolved during solution treatment with a nano-sized single-cubic-ordering phase was precipitated caused by spinodal decomposition [40]. The SEBM manufacture of Al0.5CrMoNbTa0.5 HEA using a blend of elemental powders can be possible through the optimization of the process parameters as shown by Popov et al. [18].

The mechanical properties of the EBM- fabricated CoCrFeNiMn HEA parts displayed similar tensile properties as in as-casted condition and were studied by Wang et al. [61]. The predominant deformation mechanism was dislocation with the less contribution of twinning.

The EBM-fabricated AlCoCrFeNi HEA showed relatively lower strength and ductility than in as-cast conditions (Fig. 5) [58]. The fracture strength is six times higher than a conventional engineering material SUS304 and equal to 1400 MPa for EBM samples. In addition, such properties were observed for samples whose cylinder axes were parallel and perpendicular to the build direction and, which approve its anisotropic behaviour [58]. Moreover, the higher tensile strength and ductility in heat-treated EBM-fabricated Co1.5CrFeNi1.5Ti0.5Mo0.1 HEA is superior to the as-cast sample found by Fujieda et al. [40].

2.2 Laser Beam Processes

As was shown in [62], selective laser melting (SLM)-fabricated AlCoCrFeNi HEA reveals a dual-phase structure with epitaxial growth of columnar disordered BCC phases and ordered BCC phases (B2) precipitation. The increase in volumetric energy density (VED) caused an increase in the B2 phase fraction [62]. The chemical composition of the powder has a critical effect on the morphology and quality of

the final product as well. For example, with an increase in Ni content, the microstructure of AlCrCuFeNix HEA SLM manufactured is changed from columnar to equiaxed grains structure [63]. The SLM-fabricated AlCr- CuFeNi3.0 HEA reveal heterogeneous microstructures consisting of nano-sized lamellar dual-phase FCC and B2 structures, twins, and the coherently precipitated BCC nanophase within the B2 phase [63]. The SLM-printed CoCrFeNi HEA studied by Lin et al. [64] possesses columnar grain microstructure with cellular structures and a large number of dislocations at grain boundaries (Fig. 6 a,b). Heat treatment at 1300 °C for 2 h caused to the formation of equiaxed grains (Fig 6c), and twins (fig 7 a,b).

The most common CoCrFeMnNi Cantor HEA is used for powder-based additive manufacturing. It showed FCC crystal structure as in as-cast condition and SLM also [65]. There are different results concerning the microstructure of SLM-fabricated CoCrFeMnNi, i.e the columnar microstructure of the alloy along the build direction [48] or the mixed morphology of columnar and equiaxed grains [66] are reported. Further, the authors have used laser-based AM at laser power in the range of 600–1000W manufacturing of equiatomic CoCrFeMnNi HEAs [66]. There has been found that higher laser power led to a decrease in porosity and then an increase in density of the sample. The fabricated alloy showed mixed columnar and equiaxed grain microstructure [66]. The columnar grain size changed from 2 μ to 7 μ with an increase in laser power from 600 W to 1000 W. A similar microstructure was observed in Chew et al. [49] research. After annealing at 1100 °C, the microstructure became to recrystallized grain structure [66]. The cellular structure was also registered in several works [67] [68]. In these researches, the SLM-built CoCrFeMnNi HEA possesses a uniform composition and cellular subgrains with the grain boundary angle less than 5°. Whereas the as-cast sample has coarse dendrite crystals. The dislocation pile-ups, nano twins, lattice distortion, and Mn segregation at the boundaries of the melt pool in the microstructure characterization of SLM CoCrFeMnNi is reported by Li et al. [65].

To develop an additional strain hardening mechanism in HEAs through introducing interstitial atoms, such as carbon, boron, etc. has attracted great attention [69][70]. The carbon simultaneously activated twinning-induced plasticity (TWIP) and transformation-induced plasticity (TRIP) mechanisms in metastable Fe49.5Mn30Co10Cr10C0.5 HEA as was reported in [71]. The possibility of fabricating interstitial carbon strengthened HEA using SLM process was studied in [70]. The Fe49.5Mn30Co10Cr10C0.5 HEA with hierarchical microstructure (Fig. 8(a-c)) was successfully fabricated by SLM. The yield strength (~710 MPa), tensile strength (1000 MPa) and elongation at failure (28%) of the manufactured sample were much higher than those of coarse grain as-casted one [71]. The deformed samples microstructure showed planar slip bands, deformation twins, and phase transformation at the early stage of straining (Fig. 8(d-f)). At further straining the

intersected stacking faults (SFs) and slip bands were registered (Fig. 8(g)). These multiple deformation peculiarities were stated to be favorable for work-hardening behavior and lead to notable strength–ductility enhancement.

3. Wire arc additive manufacturing

Firstly, it is conditioned by the cost-effectiveness of the WAAM. The heating source in such a scheme is an electric arc. For filler material is used welding wire. The combination of these two factors gives valuable benefit and gain before high-energy laser or electron beam tools. Direct energy deposition attracts more and more attention in additive manufacturing design research. Considering gas metal arc welding (GMAW) as the most widespread it should be taken into account the operating mode. This means special welding current, voltage, welding speed, etc.

As shown in [72] the gas tungsten arc (GTA) WAAM with pre-alloyed wire can be a suitable alternative manufacturing route for the Al0.1CoCrFeNi HEA with predetermined composition. The microstructure characterization, and mechanical testing results have proved the efficiency of WAAM for HEAs. The results obtained by the authors have shown that the energy density is identified as the primary factor governing the bead continuity, and an energy density higher than 80 J/mm3 is required to deposit a uniform bead. For good energy density, a range of heat input conditions can be suitable with different travel speeds of welding.

The high heat input results in a faster build speed and improved material efficiency, surface quality compared to the low heat input. An extremely high heat input leads to a wide bead with a low profile. This will require more layers to be deposited to reach a determined height. The molten metal may drip at a certain deposit height is reached. It has been shown that low as well as high heat input deposits have similar yield strength (260 MPa), ultimate tensile strength (420 MPa), and ductility (45–55%), comparable to as-casted metal. The high heat input deposit has a 10% higher ductility and lower hardness than the low heat input one. This is caused by the structure formation, i.e. grain size increase. Consequently, the low heat input deposit has a slightly higher hardness due to a higher dislocation density as well. The optimal process parameters for GTA-WAAM of Al0.1CoCrFeNi high-entropy alloy have been determined as follows - 200A (Current), 2000 mm/min (wire feed speed), and 200 mm/min (travel speed). The mechanical property evaluation in this study as well as fractography is presented in fig. 9.

Another one approach in WAAM is based on a combined cord with several types of wires and reported by [73]. For the first time, a new type of combined cable wire (CCW) with multi-element composition has been designed and developed for the WAAM of non-equiatomic Al-Co-Cr-Fe-Ni high-entropy alloy [73]. These CCW are composed of 7 filaments and 5 chemical elements. Ass shown by the authors, this approach has the advantages of high deposition efficiency, self-rotation of the welding arc, and energy-saving capability (Fig 10).

The thin HEA walls were manufactured under pure argon gas using cold metal transfer technology. The microstructural characterization has revealed BCC and FCC phases, good bonding between layers, and defect-free microstructure (fig. 11). The fabricated Al-Co-Cr-Fe-Ni alloy exhibits high compression strength of 2900MPa with high elongation ~42% values and then possess both very good strength and ductility. It has been shown [73] that by varying the heat input, the microstructure and mechanical properties of this alloy can be controlled. It has been proved that the innovative CCW can be successfully used in the WAAM of the HEAs.

Thus, combination of DED GMAW with combination with welding wire opens perspectives for pushing forward the development of the HEA manufacturing. The metal powder-cored wire (MPCW) is beneficial in comparison with solid wire [72] due to difficulties of the production of last. Either drawing of the solid wire or combining several thin wires in one cord [73].

For the production of the MPCW with a diameter of 2.4 mm, an ultra-low carbon steel stripe with a size of 0.4 × 10 mm was used, the filling coefficient was 60%, and the wire construction was single-layer[74].

The introduction of cobalt, manganese, chromium, and nickel powders in the amount of 20… 25% each provides (figure 12) into the steel stripe tube provides high entropy composition of the whole wire. The filling coefficient is about 60%, and its ratio to the wire diameter is within 25 units. At a ratio of more than 27 units in the shell of the wire, there are microcracks that contribute to the destruction of the metal powder cored wire, which leads to the impossibility of its use for welding.

The manufacturing procedure scheme and creation route are presented in figure 13. The manufacturing route includes several stages, first is the formation U-shape form of the metal stripe, which is realized with the help of the forming rolls. The second is the filling of the U-shape metal stripe with metal powder mixture using a special tool, namely a funnel with a disc. The third stage is the enveloping U-shape metal stripe into o-shape one with the help of the drawing die. And the final stage is the drawing procedure aimed to get the needed wire diameter. Here there are peculiarities of the drawing process which consists of the partial reduction during drawing is not exceed 23% [75]. Hence the MPCW wire drawing route was selected as follows: d.3.8mm→d.3.4mm →d.3.0mm →d.2.75mm →d.2.4mm (the partial reduction respectively 20%→22% →16% →23%).

The VDU-506 power supply is used for metal deposition, the welding parameters were as follows, welding current 280-350A, arc voltage 32-34V, temperature between welds 200… 250°C. The additive manufacturing of the high-entropy alloy using metal powder cored wire with the GMAW process is proposed. Welding is performed in modes that provided stable combustion of the arc, which is achieved at a wire feed speed of 77-90 mm/s.

The developed MPCW, an additively manufactured three-dimensional sample of the high-entropy alloy of the Cantor doping system is grown. In total, ten layers of deposition will be performed, which made it possible to obtain a monolithic sample measuring 150x35x20 mm (fig.14).

4. AM process parameters

The most valuable point of AM is the possibility to control the final product through a bottom-up approach where the microstructure and properties of the fabricated product can be controlled through the process by intellectually choosing the process parameters [54]. As the material is being built locally by melting and solidification, the cooling rate and melt pool size can be varied by controlling process parameters such as source power, speed, etc.[54]. The final microstructure of the products is a function of additional parameters such as build atmosphere, build orientation, scanning strategy, and spacing between two adjacent lines that beam traces, in case of the beam melting. Researchers are choosing parameters such as power, scanning speed, lines spacing, and quantifying them into a common variable - "volumetric energy density (VED)", "laser energy density" and sometimes the "linear laser energy density" [76,77] in case of the laser AM. Additionally to the process parameters, the powder feedstock quality has also a significant effect on the quality of the manufactured product. Powder qualities are analyzed based on their composition, purity, and microstructure as well as particle morphology, density, size distribution, and flowability [78].

The AM process is controlled by a combination of several process parameters such as powder quality, deposition pattern, laser power and laser scan speed in the case of SLM process. The gas atomized (GA) powders is be more favorable to be hollow [79]. The stored gas in the GA particles may not escape out of the melt pool while the AM process, due to high cooling rates, and can lead to the increased porosity of the fabricated product. The deposition scheme has a significant effect on the resulting residual stress as well. As reported by Nickel et al. [80] a raster deposition scheme with the scan vector rotated by 90° between layers produces a smaller residual stress and thus a lower deflection. Concerning the final grain structure, the substrate orientation is influenced by [81].

In connection that HEAs have metastable nature, their AM is challenging, and the as-built samples usually have defects such as crack, pores, etc. as mentioned above. A number of parameters like powder composition and AM parameters need to be optimized to obtain HEA samples free of any defects. Research on the effect of VED on quality parts of AM-ed HEAs showed that low VED increased the probability of delamination between the successive layers, cracking, and porosity [ref]. Balling can occur if insufficient VED or high scanning speed [82]. An optimal level of VED at relatively slow scan speed improved layer-by-layer bonding and densification as well as the molten pool flowability. Instead, high VED resulted in the key-hole porosity and scattering of molten metals [83]. Thus, an optimized range of VED is needed to manufacture HEAs defect-free product [69].

5. Post-processing of additive manufactured HEAs

Despite the above-mentioned AM process parameters, the post-treatments have been proven to be effective for improving the mechanical properties of the AM-ed products [79,84]. The annealing heat treatment leads to the increased

ductility of SLM-manufactured Al-12Si alloy [85], despite decreasing strength, and an improved strength-ductility relation is reached. The ultrasonic post-processing leads to increasing the bending strength and bending modulus of AM-ed alloys as reported by Wu et al. [86]. Thus, the post-treatment as well as process parameters and required to be determined carefully.

The post-processing treatments of the additively manufactured HEAs such as cold deformation [87], thermomechanical processing [88], annealing [89], homogenizing [90], and aging [91], impact a positive influence on the microstructure and thus mechanical properties. In addition, the hot isostatic pressing (HIP) [92] is an elevated temperature densification process that is also an effective tool for structure enhancement (fig.15) and thus properties. It has been widely used in additive manufactured metallic components to heal defects such as hot cracking, voids [93], as well as to homogenize the microstructure [94]. The high isostatic pressure reduces the size and density of porosity, without changing the shape of the manufactured parts, due to high temperature softens the alloy, as well known.

The exploration of the deformation and annealing behaviors of high-entropy alloys with a ductile high-entropy alloy of Al0.5CoCrCuFeNi are reported in [89]. As shown by the authors, Al0.5CoCrCuFeNi had excellent workability and exhibited a large work hardening capacity in both hot forging and cold rolling. It has been shown that the main deformation and hardening mechanisms are associated with the nanotwinning deformation during cold work. Namely, the blockage by the Widmanstätten Cu-rich precipitates of local slip deformation in a space of several tens nanometers results in easy formation of nanotwins, as well as low stacking fault energy. Also, it was shown that Al0.5CoCrCuFeNi have higher resistances to static anneal softening than traditional alloys with comparable melting points during annealed in 5 h at 900 °C. This resistance is attributable by the authors [89] to extensive solution hardening, low stacking fault energy, and the effect of sluggish diffusion.

The microstructure and electrochemical corrosion behavior of FeCoNiCrCu0.5 HEAs annealed at various temperatures were studied by [95]. The effects of annealing temperatures of 350 °C, 650 °C, 950 °C, and 1250 °C with a holding time of 24 h at each temperature on the alloy microstructure and properties were shown. The XRD spectra of the initial sample and heat-treated to 1250 °C showed an FCC solid-solution phase. This HEA contained a matrix, with a Cu-depleted phase, a Cr-rich phase (second structure), and a Cu-rich phase (third structure). Authors have found that the Cr-rich phase precipitated in the matrix after annealing at 1250 °C and spinodal decomposition of the Cu-rich in the annealing temperature from 350 °C to 1250 °C. The electrochemical corrosion behaviors of the as-cast and annealed specimens have shown that it was severely corroded in 3.5% NaCl solution caused by precipitation of the Cu-rich phase in the matrix. The Cl^- ions preferentially attacked Cu-rich phase which is attributed to the fact that the presence of copper in the alloy degraded the corrosion resistance by pitting.

The microstructure and mechanical properties of AlxCoCrFeNi HEAs were systematically studied in [90]. The post-processing treatment of homogenization

and deformation has been applied for HEAs with varied Al content. It has been shown that single FCC and single BCC solutions, and duplex FCC–BCC are principal phases in these alloys. The spinodal decomposition of Al–Ni phases is the major reaction during the homogenization of the AlxCoCrFeNi HEAs were considered. It has been shown that there is no stress-induced phase transformation during 50%-rolling deformation, and the main strengthening mechanism is work hardening and the hardening ability of FCC was about twice that of BCC in this alloy system [90].

In other work [87], the face-centered cubic Al0.3CoCrFeNi HEA was nanostructured by post-processing treatment with high-pressure torsion (HPT). It was revealed that the HPT of this alloy exhibits a higher hardness increment than most single-phase materials, a combination of HPT and annealing significantly strengthens the HEA hardness owing to the formation of an ordered body-centered cubic secondary phase, and after HPT and annealing is ~4 times highest hardness over for the as-cast HEA.

To transform the coarse dendritic structure to the cast AlCuCrFeNiCo HEA the extensive multistep forging at 950 °C was applied by [88] to form a fine equiaxed duplex structure consisting of the mixture of BCC and FCC phases. They have shown that hot forging post-processing treatment of the HEA made it stronger and more ductile during testing at room temperature, than the as-cast alloy. Namely, the yield stress, ultimate tensile strength, and tensile ductility of the post-processed metal were 1040 MPa, 1170 MPa, and 1%, respectively, against 790 MPa, 790 MPa, and 0.2% for the as-cast condition. In the as-cast condition brittle to ductile transition occurred between 700 and 800 °C, while in the forged condition, it was observed between 600 and 700 °C. Authors have found [88] that in the temperature range of 800–1000 °C, the post-processed alloy showed superplastic behavior with elongation above 400% and even reached 860% at 1000 °C.

The microstructure evolution in CoCrFeNiMn HEA during uniaxial compression to a height reduction corresponding to the true strain of ≈1.4 in the temperature interval 600–1100 °C was studied in [96]. The differences in the mechanical behavior of the alloy and the activation energy of deformation below and above 800 °C temperature intervals were observed. It has been shown that microstructure evolution at studied temperatures was found to be accompanied by discontinuous dynamic recrystallization (DDRX). The DRX was primarily associated with the nucleation of new grains on the initial grain boundaries, during hot deformation. When in the warm interval DDRX was mainly observed in shear bands. In this case, the volume fraction of the recrystallized structure was 0.085 at 600 °C and 0.95 at 1000 °C, with the grain sizes of 0.2 and 40.4 μm, respectively.

6. Conclusions

In summary, high entropy alloys (HEAs) exhibit a range of advantages, making them highly appealing in various applications. Additive manufacturing (AM) tech-

niques have emerged as a promising approach for fabricating HEAs, offering distinct advantages over conventional methods. Additionally, AM software provides the capability to simulate printing processes, including the melting pool and AM techniques, allowing for improved process optimization. While this review does not delve into the specifics of such simulations, they hold potential for enhancing future research endeavors.

Comparisons of AM process parameters, particularly volumetric energy density (VED), among different techniques enable a deeper understanding of their effects on HEA fabrication. This knowledge aids in selecting the most suitable AM technique for specific applications and optimizing the resulting material properties.

Regarding post-processing after AM, considerations such as the necessity of hot isostatic pressing (HIP) or the sufficiency of simple annealing depend on the desired material characteristics and application requirements. These factors should be carefully evaluated to achieve the desired performance of the final HEA product.

Looking ahead, promising prospects include the exploration of novel HEAs with unique compositions and properties, as well as the investigation of underutilized AM techniques for HEA fabrication. Additionally, identifying new applications that can leverage the exceptional attributes of HEAs in additive manufacturing holds significant potential for advancing the field.

In conclusion, this review highlights the advantages of HEAs, the benefits of AM techniques over conventional methods, the potential of AM software for simulation, the importance of process parameters, the significance of post-processing considerations, and the prospects for future advancements in HEA research and applications.

References

1. P. Ashtari, K. Tetley-Gerard, K. Sadayappan, Removal of iron from recycled aluminium alloys, *Can. Metall. Q.,* **51:** 75–80 (2012)
2. J.-W. Yeh, S.-K. Chen, S.-J. Lin, J.-Y. Gan, T.-S. Chin, T.-T. Shun, C.-H. Tsau, S.-Y. Chang, Nanostructured High-Entropy Alloys with Multiple Principal Elements: Novel Alloy Design Concepts and Outcomes, *Adv. Eng. Mater.*, **6**: 299–303 (2004). https://doi.org/10.1002/adem.200300567.
3. B. Cantor, I.T.H. Chang, P. Knight, and A.J.B. Vincent, Microstructural development in equiatomic multicomponent alloys, *Mater. Sci. Eng. A*, **375–377**: 213–218 (2004). https://doi.org/10.1016/j.msea.2003.10.257.
4. S. Chen, Y. Tong, and P.K. Liaw, Additive manufacturing of high-entropy alloys: a review, *Entropy*, **20**: 937 (2018).
5. Z. Wu, H. Bei, G.M. Pharr, and E.P. George, Temperature dependence of the mechanical properties of equiatomic solid solution alloys with face-centered cubic crystal structures, *Acta Mater.*, **81**: 428–441 (2014). https://doi.org/10.1016/j.actamat.2014.08.026.
6. E. Johnson, Cohesion in metals: (Cohesion and structure, vol. 1) by F.R. de Boer, R. Boom, W.C.M. Mattens, A.R. Miedema and A.K. Niessen (Elsevier, Amsterdam, 1988) pp.

xiv + 758, hardbound, US $ 131.50/Dfl 250-. ISBN 0-444-87098-9, Nucl. Instruments Methods Phys. Res. Sect. B Beam Interact. with Mater. Atoms. **42**: 403 (1989). https://doi.org/10.1016/0168-583X(89)90456-4.

7. K. Wu, N. Ding, T. Yin, M. Zeng, Z. Liang, Effects of single and double pulses on microstructure and mechanical properties of weld joints during high-power double-wire GMAW, *J. Manuf. Process.*, **35:** 728–734 (2018). https://doi.org/10.1016/j.jmapro.2018.08.025.
8. G. Bernd, H. Anton, C. Dhiraj, C.E. H., G.E. P., R.R. O., A fracture-resistant high-entropy alloy for cryogenic applications, *Science (80-.),* **345:** 1153–1158 (2014). https://doi.org/10.1126/science.1254581 .
9. A. Takeuchi, K. Amiya, T. Wada, K. Yubuta, W. Zhang, High-Entropy Alloys with a Hexagonal Close-Packed Structure Designed by Equi-Atomic Alloy Strategy and Binary Phase Diagrams, *JOM.*, **66:** 1984–1992 (2014). https://doi.org/10.1007/s11837-014-1085-x.
10. C.L. Tracy, S. Park, D.R. Rittman, S.J. Zinkle, H. Bei, M. Lang, R.C. Ewing, W.L. Mao, High pressure synthesis of a hexagonal close-packed phase of the high-entropy alloy CrMnFeCoNi, *Nat. Commun.,* **8:** 15634 (2017). https://doi.org/10.1038/ncomms15634.
11. Y.-J. Liang, L. Wang, Y. Wen, B. Cheng, Q. Wu, T. Cao, Q. Xiao, Y. Xue, G. Sha, Y. Wang, Y. Ren, X. Li, L. Wang, F. Wang, H. Cai, High-content ductile coherent nanoprecipitates achieve ultrastrong high-entropy alloys, *Nat. Commun.***, 9:** 4063 (2018). https://doi.org/10.1038/s41467-018-06600-8.
12. W. Ji, W. Wang, H. Wang, J. Zhang, Y. Wang, F. Zhang, Z. Fu, Short communication, Intermetallics. **56**, 24–27 ,(2015). https://doi.org/10.1016/j.intermet.2014.08.008.
13. Z. Tang, T. Yuan, C.-W. Tsai, J.-W. Yeh, C.D. Lundin, P.K. Liaw, Fatigue behavior of a wrought Al0.5CoCrCuFeNi two-phase high-entropy alloy, *Acta Mater.*, **99:** 247–258 (2015) https://doi.org/10.1016/j.actamat.2015.07.004.
14. Y. ZHOU, Y. ZHANG, X. WANG, Y. WANG, G. CHEN, Effect of component substitution on the microstructure and mechanical properties of MCoCrFeNiTix (M = Cu, Al) solid-solution alloys, *Rare Met.*, **27:** 627–631 (2008). https://doi.org/10.1016/S1001-0521(08)60195-3.
15. W.H. Liu, Y. Wu, J.Y. He, T.G. Nieh, Z.P. Lu, Grain growth and the Hall–Petch relationship in a high-entropy FeCrNiCoMn alloy, *Scr. Mater.***, 68:** 526–529 (2013). https://doi.org/10.1016/j.scriptamat.2012.12.002.
16. O.N. Senkov, G.B. Wilks, J.M. Scott, D.B. Miracle, Mechanical properties of Nb25Mo25Ta25W25 and V20Nb20Mo20Ta20W20 refractory high entropy alloys, *Intermetallics.*, **19:** 698–706 (2011). https://doi.org/10.1016/j.intermet.2011.01.004.
17. J.M. Park, J. Choe, J.G. Kim, J.W. Bae, J. Moon, S. Yang, K.T. Kim, J.-H. Yu, H.S. Kim, Superior tensile properties of 1%C-CoCrFeMnNi high-entropy alloy additively manufactured by selective laser melting, *Mater. Res. Lett.*, **8:** 1–7 (2020). https://doi.org/10.1080/21663831.2019.1638844.
18. F. Zhang, S. Zhao, K. Jin, H. Bei, D. Popov, Pressure-induced fcc to hcp phase transition in Ni-based high entropy solid solution alloys, *Appl. Phys. Lett.*, **110:** 011902 (2017). https://doi.org/DOI:101063/14973627.
19. S. Mridha, M. Sadeghilaridjani, S. Mukherjee, Activation Volume and Energy for Dislocation Nucleation in Multi-Principal Element Alloys, *Met.*, **9:** 263 (2019). https://doi.org/10.3390/met9020263.
20. Y. Zhang, Y.J. Zhou, J.P. Lin, G.L. Chen, P.K. Liaw, Solid-Solution Phase Formation Rules for Multi-component Alloys, *Adv. Eng. Mater.*, **10:** 534–538 (2008). https://doi.org/10.1002/adem.200700240.

21. C. Zhu, Z.P. Lu, T.G. Nieh, Incipient plasticity and dislocation nucleation of FeCoCrNiMn high-entropy alloy, *Acta Mater.*, **61:** 2993–3001 (2013). https://doi.org/10.1016/j.actamat.2013.01.059.
22. Y. Brif, M. Thomas, I. Todd, The use of high-entropy alloys in additive manufacturing, *Scr. Mater.*, **99:** 93-96 (2015). https://doi.org/10.1016/j.scriptamat.2014.11.037 .
23. Y. Deng, C.C. Tasan, K.G. Pradeep, H. Springer, A. Kostka, D. Raabe, Design of a twinning-induced plasticity high entropy alloy, *Acta Mater.,* **94:** 124–133 (2015). https://doi.org/10.1016/j.actamat.2015.04.014.
24. C. Li, J.C. Li, M. Zhao, Q. Jiang, Effect of alloying elements on microstructure and properties of multiprincipal elements high-entropy alloys, *J. Alloys Compd.*, **475:** 752–757 (2009). https://doi.org/10.1016/j.jallcom.2008.07.124.
25. O.N. Senkov, J.M. Scott, S. V Senkova, D.B. Miracle, C.F. Woodward, Microstructure and room temperature properties of a high-entropy TaNbHfZrTi alloy, *J. Alloys Compd.*, **509:** 6043–6048 (2011). https://doi.org/10.1016/j.jallcom.2011.02.171.
26. N.N. Guo, L. Wang, L.S. Luo, X.Z. Li, Y.Q. Su, J.J. Guo, H.Z. Fu, Microstructure and mechanical properties of refractory MoNbHfZrTi high-entropy alloy, *Mater. Des.*, **81**, 87–94, (2015). https://doi.org/10.1016/j.matdes.2015.05.019.
27. S. Maiti, W. Steurer, Structural-disorder and its effect on mechanical properties in single-phase TaNbHfZr high-entropy alloy, *Acta Mater.*, **106:** 87–97 (2016) https://doi.org/10.1016/j.actamat.2016.01.018 .
28. M.C. Gao, B. Zhang, S.M. Guo, J.W. Qiao, J.A. Hawk, High-Entropy Alloys in Hexagonal Close-Packed Structure, *Metall. Mater. Trans. A.*, **47:** 3322 (2016). https://doi.org/10.1007/s11661-015-3091-1.
29. Z. Li, K.G. Pradeep, Y. Deng, D. Raabe, C.C. Tasan, Metastable high-entropy dual-phase alloys overcome the strength–ductility trade-off, *Nature.*, **534:** 227–230., (2016). https://doi.org/10.1038/nature17981.
30. J.M. Zhu, H. Fu, H. Zhang, A.M. Wang, H. Li, Z. Hu, Microstructures and compressive properties of multicomponent AlCoCrFeNiMo x alloys, *Mater. Sci. Eng. A.*, **527:** 6975–6979 (2010). https://doi.org/10.1016/j.msea.2010.07.028.
31. G. Laplanche, A. Kostka, O.M. Horst, G. Eggeler, E.P. George, Microstructure evolution and critical stress for twinning in the CrMnFeCoNi high-entropy alloy, *Acta Mater.*, **118:** 152–163 (2016). https://doi.org/10.1016/j.actamat.2016.07.038.
32. M.J. Jang, S.-H. Joo, C.-W. Tsai, J.-W. Yeh, H. Kim, Compressive deformation behavior of CrMnFeCoNi high-entropy alloy, *Met. Mater. Int.*, **22:** 982–986 (2016). https://doi.org/10.1007/s12540-016-6304-2.
33. M. Chinababu, N. Naga Krishna, K. Sivaprasad, K.G. Prashanth, E. Bhaskara Rao, Evolution of microstructure and mechanical properties of LM25–HEA composite processed through stir casting with a bottom pouring system, *Materials (Basel),* **15:** 230 (2022).
34. Q.H. Li, T.M. Yue, Z.N. Guo, X. Lin, Microstructure and corrosion properties of AlCoCrFeNi high entropy alloy coatings deposited on AISI 1045 steel by the electrospark process, *Metall. Mater. Trans. A.*, **44:** 1767–1778 (2013).
35. N. Eißmann, B. Klöden, T. Weißgärber, B. Kieback, High-entropy alloy CoCrFeMnNi produced by powder metallurgy, *Powder Metall.*, **60:** 184–197 (2017).
36. Y. Wang, T. Voisin, J. McKeown, J. Ye, N. Calta, Z. Li, Z. Zeng, Y. Zhang, W. Chen, T. Roehling, R. Ott, M. Santala, P.J. Depond, M. Matthews, A. Hamza, T. Zhu, Additively manufactured hierarchical stainless steels with high strength and ductility, *Nat. Mater.*, **17:** 63-71 (2018). https://doi.org/10.1038/nmat5021.

37. W. Xu, E.W. Lui, A. Pateras, M. Qian, M. Brandt, In situ tailoring microstructure in additively manufactured Ti-6Al-4V for superior mechanical performance, *Acta Mater.*, **125:** 390–400 (2017). https://doi.org/10.1016/j.actamat.2016.12.027.
38. W. Xu, M. Brandt, S. Sun, J. Elambasseril, Q. Liu, K. Latham, K. Xia, M. Qian, Additive manufacturing of strong and ductile Ti–6Al–4V by selective laser melting via in situ martensite decomposition, *Acta Mater.*, **85:** 74–84 (2015). https://doi.org/10.1016/j.actamat.2014.11.028.
39. R. Zhou, Y. Liu, B. Liu, L. Jia, Q. Fang, Precipitation behavior of selective laser melted FeCoCrNiC 0.05 high entropy alloy, *Intermetallics.*, **106:** 20-25 (2019). https://doi.org/10.1016/j.intermet.2018.12.001.
40. T. Fujieda, H. Shiratori, K. Kuwabara, M. Hirota, T. Kato, K. Yamanaka, Y. Koizumi, A. Chiba, S. Watanabe, CoCrFeNiTi-based high-entropy alloy with superior tensile strength and corrosion resistance achieved by a combination of additive manufacturing using selective electron beam melting and solution treatment, *Mater. Lett.*, **189:** 148–151 (2017). https://doi.org/10.1016/j.matlet.2016.11.026.
41. X.H. An, X. Liao, Z.G. Zhu, B. Nguyen, F. Ng, P.K. Liaw, M.L.S. Nai, J. Wei, Hierarchical microstructure and strengthening mechanisms of a CoCrFeNiMn high entropy alloy additively manufactured by selective laser melting, *Scr. Mater.*, **154:** 20-24 (2018). https://doi.org/10.1016/j.scriptamat.2018.05.015.
42. A. Piglione, B. Dovgyy, C. Liu, C.M. Gourlay, P.A. Hooper, M.S. Pham, Printability and microstructure of the CoCrFeMnNi high-entropy alloy fabricated by laser powder bed fusion, *Mater. Lett.*, **224:** 22–25 (2018). https://doi.org/10.1016/j.matlet.2018.04.052 .
43. W. Wu, R. Zhou, B. Wei, S. Ni, Y. Liu, M. Song, Nanosized precipitates and dislocation networks reinforced C-containing CoCrFeNi high-entropy alloy fabricated by selective laser melting, *Mater. Charact.*, **144:** 605–610 (2018). https://doi.org/DOI:101016/jmatchar201808019.
44. T. Borkar, V. Chaudhary, B. Gwalani, D. Choudhuri, C. V Mikler, V. Soni, T. Alam, R. V. Ramanujan, R. Banerjee, A Combinatorial Approach for Assessing the Magnetic Properties of High Entropy Alloys: Role of Cr in AlCoxCr1–xFeNi , *Adv. Eng. Mater.*, **19:** 1700048 (2017). https://doi.org/10.1002/adem.201700048.
45. B. Zheng, Y. Zhou, J.E. Smugeresky, J.M. Schoenung, E. Lavernia, Thermal Behavior and Microstructural Evolution during Laser Deposition with Laser-Engineered Net Shaping: Part I. Numerical Calculations, *Metall. Mater. Trans. A.*, **39:** 2228–2236 (2008). https://doi.org/10.1007/s11661-008-9557-7.
46. Z. Sun, X. Tan, M. Descoins, D. Mangelinck, S. Tor, C. Lim, Revealing hot tearing mechanism for an additively manufactured high-entropy alloy via selective laser melting, *Scr. Mater.*, **168:** 129–133 (2019). https://doi.org/10.1016/j.scriptamat.2019.04.036.
47. C. Haase, F. Tang, M.B. Wilms, A. Weisheit, B. Hallstedt, Combining thermodynamic modeling and 3D printing of elemental powder blends for high-throughput investigation of high-entropy alloys – Towards rapid alloy screening and design, *Mater. Sci. Eng. A.*, **688:** 180–189 (2017) https://doi.org/10.1016/j.msea.2017.01.099.
48. Z. Qiu, C. Yao, K. Feng, Z. Li, P. Chu, Cryogenic deformation mechanism of CrMnFeCoNi high-entropy alloy fabricated by laser additive manufacturing process, *Int. J. Light. Mater. Manuf.*, **1**: 33-39 (2018). https://doi.org/10.1016/j.ijlmm.2018.02.001.
49. Y. Chew, G. Bi, Z.G. Zhu, F. Ng, F. Weng, S. Liu, M.L.S. Nai, B.Y. Lee, Microstructure and Enhanced Strength of Laser Aided Additive Manufactured CoCrFeNiMn High Entropy Alloy, *Mater. Sci. Eng. A.*, **744:** 137-144 (2018). https://doi.org/10.1016/j.msea.2018.12.005.

50. M. Moorehead, K. Bertsch, M. Niezgoda, C. Parkin, M. Elbakhshwan, K. Sridharan, C. Zhang, D. Thoma, A. Couet, High-throughput synthesis of Mo-Nb-Ta-W high-entropy alloys via additive manufacturing, *Mater. Des.*, **187:** 108358 (2020) https://doi.org/10.1016/j.matdes.2019.108358.
51. H. Dobbelstein, E.L. Gurevich, E.P. George, A. Ostendorf, G. Laplanche, Laser metal deposition of compositionally graded TiZrNbTa refractory high-entropy alloys using elemental powder blends, *Addit. Manuf.*, **25:** 252–262 (2019). https://doi.org/10.1016/j.addma.2018.10.042.
52. I. Kunce, M. Polanski, J. Bystrzycki, Structure and hydrogen storage properties of a high entropy ZrTiVCrFeNi alloy synthesized using Laser Engineered Net Shaping (LENS), *Int. J. Hydrogen Energy.*, **38:** 12180–12189 (2013). https://doi.org/10.1016/j.ijhydene.2013.05.071.
53. P.K. Sarswat, S. Sarkar, A. Murali, W. Huang, W. Tan, M.L. Free, Additive manufactured new hybrid high entropy alloys derived from the AlCoFeNiSmTiVZr system, *Appl. Surf. Sci.*, **476:** 242–258 (2019). https://doi.org/10.1016/j.apsusc.2018.12.300.
54. L. Ladani, M. Sadeghilaridjani, Review of Powder Bed Fusion Additive Manufacturing for Metals, *Met.*, **11**: 1391 (2021). https://doi.org/10.3390/met11091391.
55. M. Sadeghilaridjani, S. Muskeri, V. Hasannaeimi, M. Pole, S. Mukherjee, Strain rate sensitivity of a novel refractory high entropy alloy: Intrinsic versus extrinsic effects, *Mater. Sci. Eng. A.*, **766:** 138326 (2019). https://doi.org/10.1016/j.msea.2019.138326.
56. P.J. Barron, A.W. Carruthers, J.W. Fellowes, N.G. Jones, H. Dawson, E.J. Pickering, Towards V-based high-entropy alloys for nuclear fusion applications, *Scr. Mater.*, **176:** 12–16 (2020). https://doi.org/10.1016/j.scriptamat.2019.09.028.
57. T. Yang, Y.L. Zhao, J.H. Luan, B. Han, J. Wei, J.J. Kai, C.T. Liu, Nanoparticles-strengthened high-entropy alloys for cryogenic applications showing an exceptional strength-ductility synergy, *Scr. Mater.*, **164:** 30–35 (2019). https://doi.org/10.1016/j.scriptamat.2019.01.034.
58. T. Fujieda, H. Shiratori, K. Kuwabara, T. Kato, K. Yamanaka, Y. Koizumi, A. Chiba, First demonstration of promising selective electron beam melting method for utilizing high-entropy alloys as engineering materials, *Mater. Lett.*, **159:** 12–15 (2015) https://doi.org/10.1016/j.matlet.2015.06.046 .
59. K. Kuwabara, H. Shiratori, T. Fujieda, K. Yamanaka, Y. Koizumi, A. Chiba, Mechanical and corrosion properties of AlCoCrFeNi high-entropy alloy fabricated with selective electron beam melting, *Addit. Manuf.*, **23:** 264–271 (2018). https://doi.org/10.1016/j.addma.2018.06.006.
60. H. Shiratori, T. Fujieda, K. Yamanaka, Y. Koizumi, K. Kuwabara, T. Kato, A. Chiba, Relationship between the microstructure and mechanical properties of an equiatomic AlCoCrFeNi high-entropy alloy fabricated by selective electron beam melting, *Mater. Sci. Eng. A.*, **656:** 39–46 (2016) https://doi.org/10.1016/j.msea.2016.01.019.
61. P. Wang, P. Huang, F.L. Ng, W.J. Sin, S. Lu, M.L.S. Nai, Z. Dong, J. Wei, Additively manufactured CoCrFeNiMn high-entropy alloy via pre-alloyed powder, *Mater. Des.*, **168:** 107576 (2019). https://doi.org/10.1016/j.matdes.2018.107576.
62. P.D. Niu, R.D. Li, T.C. Yuan, S.Y. Zhu, C. Chen, M.B. Wang, L. Huang, Microstructures and properties of an equimolar AlCoCrFeNi high entropy alloy printed by selective laser melting, *Intermetallics.*, **104**: 24–32 (2019). https://doi.org/10.1016/j.intermet.2018.10.018.
63. S. Luo, C. Zhao, Y. Su, Q. Liu, Z. Wang, Selective laser melting of dual phase AlCrCuFeNix high entropy alloys: Formability, heterogeneous microstructures and deformation

mechanisms, *Addit. Manuf.*, **31**: 100925 (2020). https://doi.org/10.1016/j.addma.2019.100925.
64. D. Lin, L. Xu, H. Jing, Y. Han, L. Zhao, F. Minami, Effects of annealing on the structure and mechanical properties of FeCoCrNi high-entropy alloy fabricated via selective laser melting, *Addit. Manuf.*, **32:** 101058 (2020). https://doi.org/10.1016/j.addma.2020.101058.
65. R. Li, P. Niu, T. Yuan, P. Cao, C. Chen, K. Zhou, Selective laser melting of an equiatomic CoCrFeMnNi high-entropy alloy: Processability, non-equilibrium microstructure and mechanical property, *J. Alloys Compd.*, **746:** 125–134 (2018). https://doi.org/10.1016/j.jallcom.2018.02.298.
66. Z. Tong, X. Ren, J. Jiao, W. Zhou, Y. Ren, Y. Ye, E.A. Larson, J. Gu, Laser additive manufacturing of FeCrCoMnNi high-entropy alloy: Effect of heat treatment on microstructure, residual stress and mechanical property, *J. Alloys Compd.*, **785:** 1144–1159 (2019) https://doi.org/10.1016/j.jallcom.2019.01.213.
67. Z. Xu, H. Zhang, X. Du, Y. He, H. Luo, G. Song, L. Mao, T. Zhou, L. Wang, Corrosion resistance enhancement of CoCrFeMnNi high-entropy alloy fabricated by additive manufacturing, *Corros. Sci.*, **177:** 108954 (2020). https://doi.org/10.1016/j.corsci.2020.108954.
68. Z. Xu, H. Zhang, W. Li, A. Mao, L. Wang, G. Song, Y. He, Microstructure and nanoindentation creep behavior of CoCrFeMnNi high-entropy alloy fabricated by selective laser melting, *Addit. Manuf.*, **28:** 766–771 (2019). https://doi.org/10.1016/j.addma.2019.06.012.
69. A. Ostovari Moghaddam, N.A. Shaburova, M.N. Samodurova, A. Abdollahzadeh, E.A. Trofimov, Additive manufacturing of high entropy alloys: A practical review, *J. Mater. Sci. Technol.*, **77:** 131–162 (2021). https://doi.org/10.1016/j.jmst.2020.11.029.
70. Z. Zhu, X.H. An, W. Lu, Z. Li, F. Ng, X. Liao, U. Ramamurty, M.L.S. Nai, J. Wei, Selective laser melting enabling the hierarchically heterogeneous microstructure and excellent mechanical properties in an interstitial solute strengthened high entropy alloy, *Mater. Res. Lett.*, **7:** 453-459 (2019). https://doi.org/10.1080/21663831.2019.1650131.
71. Z. Li, C.C. Tasan, H. Springer, B. Gault, D. Raabe, Interstitial atoms enable joint twinning and transformation induced plasticity in strong and ductile high-entropy alloys, *Sci. Rep.*, **7:** 40704 (2017). https://doi.org/10.1038/srep40704.
72. M.R.U. Ahsan, G.-J. Seo, X. Fan, P.K. Liaw, S. Motaman, C. Haase, D.B. Kim, Effects of process parameters on bead shape, microstructure, and mechanical properties in wire + arc additive manufacturing of Al0.1CoCrFeNi high-entropy alloy, *J. Manuf. Process.,* **68:** 1314–1327 (2021). https://doi.org/10.1016/j.jmapro.2021.06.047.
73. Q. Shen, X. Kong, X. Chen, Fabrication of bulk Al-Co-Cr-Fe-Ni high-entropy alloy using combined cable wire arc additive manufacturing (CCW-AAM): Microstructure and mechanical properties, *J. Mater. Sci. Technol.*, **74:** 136–142 (2021). https://doi.org/10.1016/j.jmst.2020.10.037.
74. A. Zavdoveev, A. Klapatyuk, T. Baudin, E. MacDonald, D. Mohan, J. Oliveira, A. Gajvoronskiy, V. Poznyakov, H.S. Kim, F. Brisset, M. Khokhlov, M. Heaton, M. Rogante, M. Skoryk, D. Vedel, R. Kozin, I. Klochkov, S. Motrunich, Non-equimolar Cantor high entropy alloy fabrication using metal powder cored wire arc additive manufacturing, *Addit. Manuf. Lett.*, **6:** 100124 (2023). https://doi.org/10.1016/j.addlet.2023.100124.
75. A. Zavdoveev, T. Baudin, E. Pashinska, H.S. Kim, F. Brisset, M. Heaton, V. Poznyakov, M. Rogante, V. Tkachenko, I. Klochkov, M. Skoryk, Continuous Severe Plastic Deformation of Low-Carbon Steel: Physical–Mechanical Properties and Multiscale Structure Analysis, *Steel Res. Int.*, **92:** 2000482 (2021). https://doi.org/10.1002/srin.202000482.

76. N.H. Sateesh, G.C.M. Kumar, K. Prasad, S. C.K., A.R. Vinod, Microstructure and Mechanical Characterization of Laser Sintered Inconel-625 Superalloy, *Procedia Mater. Sci.,* **5:** 772–779 (2014). https://doi.org/10.1016/j.mspro.2014.07.327 .
77. Q. Jia, D. Gu, Selective laser melting additive manufacturing of Inconel 718 superalloy parts: Densification, microstructure and properties, *J. Alloys Compd.*, **585:** 713–721 (2014). https://doi.org/10.1016/j.jallcom.2013.09.171.
78. J.A. Muñiz-Lerma, A. Nommeots-Nomm, K.E. Waters, M. Brochu, A Comprehensive Approach to Powder Feedstock Characterization for Powder Bed Fusion Additive Manufacturing: A Case Study on AlSi7Mg, *Mater.*, **11:** 2386 (2018). https://doi.org/10.3390/ma11122386.
79. X. Zhao, J. Chen, X. Lin, W. Huang, Study on microstructure and mechanical properties of laser rapid forming Inconel 718, *Mater. Sci. Eng. A.*, **478:** 119–124 (2008). https://doi.org/10.1016/j.msea.2007.05.079.
80. A.H. Nickel, D.M. Barnett, F.B. Prinz, Thermal stresses and deposition patterns in layered manufacturing, *Mater. Sci. Eng. A.*, **317:** 59–64 (2001). https://doi.org/10.1016/S0921-5093(01)01179-0.
81. L. Wang, N. Wang, W.J. Yao, Y. Zheng, Effect of substrate orientation on the columnar-to-equiaxed transition in laser surface remelted single crystal superalloys, *Acta Mater.*, **88:** 283-292(2015). https://doi.org/10.1016/j.actamat.2015.01.063.
82. D. Gu, Y. Shen, Balling phenomena in direct laser sintering of stainless steel powder: Metallurgical mechanisms and control methods, *Mater. Des.*, **30:** 2903–2910 (2009). https://doi.org/10.1016/j.matdes.2009.01.013.
83. D.B. Hann, J. Iammi, J. Folkes, A simple methodology for predicting laser-weld properties from material and laser parameters, *J. Phys. D. Appl. Phys.*, **44:** 445401 (2011). https://doi.org/10.1088/0022-3727/44/44/445401.
84. T. Vilaro, C. Colin, J.D. Bartout, L. Nazé, M. Sennour, Microstructural and mechanical approaches of the selective laser melting process applied to a nickel-base superalloy, *Mater. Sci. Eng. A.*, **534:** 446–451 (2012). https://doi.org/10.1016/j.msea.2011.11.092.
85. K.G. Prashanth, S. Scudino, H.J. Klauss, K.B. Surreddi, L. Löber, Z. Wang, A.K. Chaubey, U. Kühn, J. Eckert, Microstructure and mechanical properties of Al–12Si produced by selective laser melting: Effect of heat treatment, *Mater. Sci. Eng. A.*, **590:** 153–160 (2014). https://doi.org/10.1016/j.msea.2013.10.023.
86. W. Wu, J. Jiang, H. Jiang, W. Liu, G. Li, B. Wang, M. Tang, J. Zhao, Improving bending and dynamic mechanics performance of 3D printing through ultrasonic strengthening, *Mater. Lett.* **220:** 317–320 (2018). https://doi.org/10.1016/j.matlet.2018.03.048.
87. Q.H. Tang, Y. Huang, Y.Y. Huang, X.Z. Liao, T.G. Langdon, P.Q. Dai, Hardening of an Al0.3CoCrFeNi high entropy alloy via high-pressure torsion and thermal annealing, *Mater. Lett.*, **151:** 126–129 (2015). https://doi.org/10.1016/j.matlet.2015.03.066.
88. A. V Kuznetsov, D.G. Shaysultanov, N.D. Stepanov, G.A. Salishchev, O.N. Senkov, Tensile properties of an AlCrCuNiFeCo high-entropy alloy in as-cast and wrought conditions, *Mater. Sci. Eng. A.*, **533:** 107–118 (2012). https://doi.org/10.1016/j.msea.2011.11.045.
89. C.-W. Tsai, Y.-L. Chen, M.-H. Tsai, J.-W. Yeh, T.-T. Shun, S.-K. Chen, Deformation and annealing behaviors of high-entropy alloy Al0.5CoCrCuFeNi, *J. Alloys Compd.*, **486:** 427–435 (2009). https://doi.org/10.1016/j.jallcom.2009.06.182.
90. Y.-F. Kao, T.-J. Chen, S.-K. Chen, J.-W. Yeh, Microstructure and mechanical property of as-cast, -homogenized, and -deformed AlxCoCrFeNi (0≤x≤2) high-entropy alloys, *J. Alloys Compd.*, **488:** 57–64 (2009). https://doi.org/10.1016/j.jallcom.2009.08.090.
91. T.-T. Shun, Y.-C. Du, Age hardening of the Al0.3CoCrFeNiC0.1 high entropy alloy, *J. Alloys Compd.*, **478:** 269–272(2009). https://doi.org/10.1016/j.jallcom.2008.12.014.

92. J. Joseph, P. Hodgson, T. Jarvis, X. Wu, N. Stanford, D.M. Fabijanic, Effect of hot isostatic pressing on the microstructure and mechanical properties of additive manufactured AlxCoCrFeNi high entropy alloys, *Mater. Sci. Eng. A.*, **733:** 59–70 (2018). https://doi.org/10.1016/j.msea.2018.07.036.
93. X. Zhao, X. Lin, J. Chen, L. Xue, W. Huang, The effect of hot isostatic pressing on crack healing, microstructure, mechanical properties of Rene88DT superalloy prepared by laser solid forming, *Mater. Sci. Eng. A.*, **504:** 129–134 (2009). https://doi.org/10.1016/j.msea.2008.12.024.
94. M.T. Kim, S.Y. Chang, J.B. Won, Effect of HIP process on the micro-structural evolution of a nickel-based superalloy, *Mater. Sci. Eng. A.*, **441:** 126–134 (2006). https://doi.org/10.1016/j.msea.2006.09.060.
95. C.-M. Lin, H.-L. Tsai, Effect of annealing treatment on microstructure and properties of high-entropy FeCoNiCrCu0.5 alloy, *Mater. Chem. Phys.*, **128:** 50–56 (2011). https://doi.org/10.1016/j.matchemphys.2011.02.022.
96. N.D. Stepanov, D.G. Shaysultanov, N.Y. Yurchenko, S. V Zherebtsov, A.N. Ladygin, G.A. Salishchev, M.A. Tikhonovsky, High temperature deformation behavior and dynamic recrystallization in CoCrFeNiMn high entropy alloy, *Mater. Sci. Eng. A.*, **636:** 188–195 (2015). https://doi.org/10.1016/j.msea.2015.03.097.

Table 1 Phases and alloying systems of some typical HEAs.

Crystalsystem	Alloy system	References
FCC	CrCoNiMn CoNiFeMn CrCoNiFe CrCoNiFePd CrMnFeCoNi FeNiCrCuCo FeNiCrCuMo Fe40Mn40Co10Cr10 FeCoCrNiC0.05 Fe50Mn30Co10Cr10	[5,18,21,23,24,29]
BCC	AlCoCrFeNiMox NbMoTaW NbMoTaW VNbMoTaW MoNbHfZrTi TaNbHfZrTi TaNbHfZr AlCoCrFeNiMox	[16,25,27,30]
HCP	YGdTbDyLu GdTbDyTmLu and CoFeReRu	[9,28]

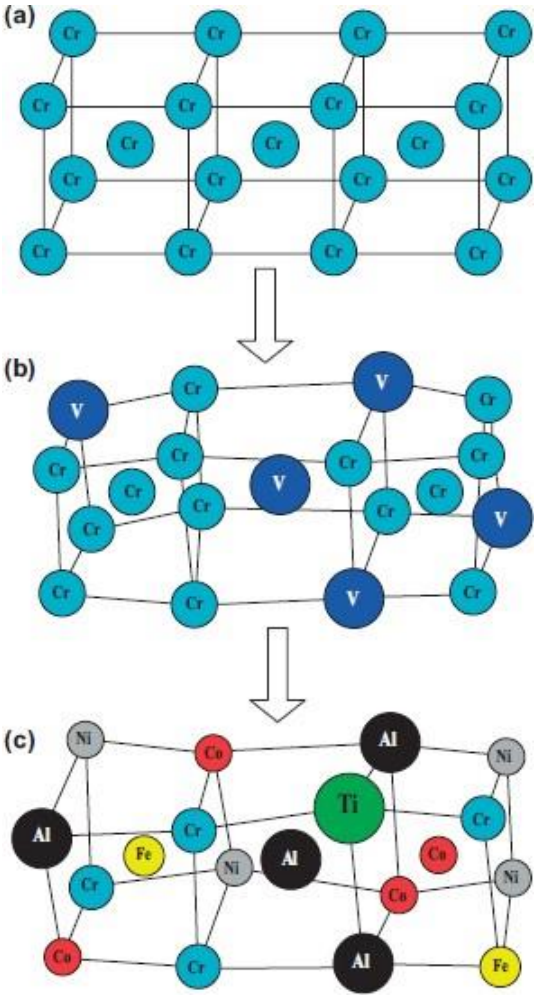

Fig. 1 Schematic illustration of severe lattice distortion of HEAs [20]: a) BCC crystal with a perfect lattice b) Distorded lattice due to the introduction of a element with different radius c) Differents elements with different radius, randomly distributed.

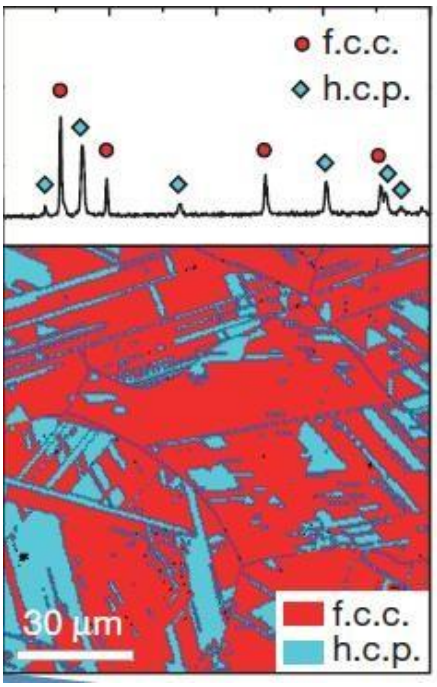

Fig. 2 XRD profile and EBSD phase map of Fe50Mn30Co10Cr10 HEA [29].

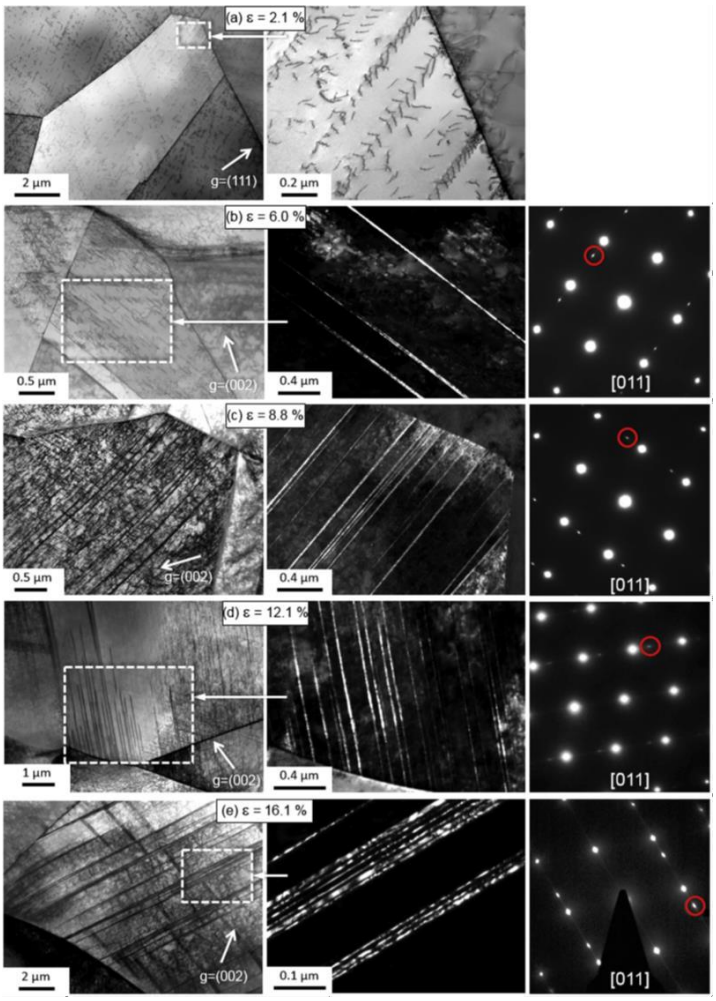

Fig. 3 The formation and hence evolution of the deformation substructures during tensile straining of CrMnFeCoNi at 77 K [31].

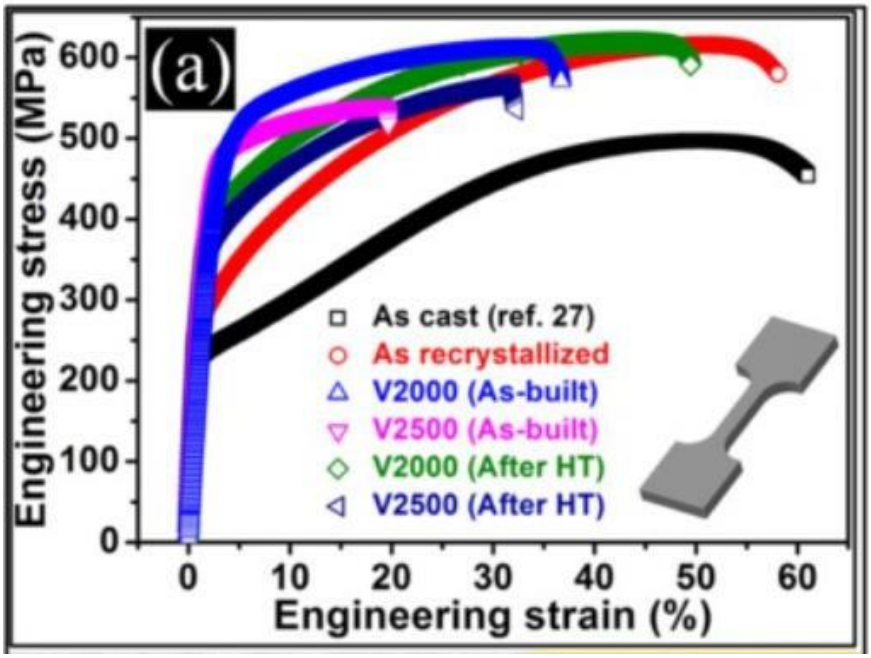

Fig. 4 The engineering stress-strain curves of the CrMnFeCoNi with different conditions [41]. Were V2000 and 2500 is velocity in mm/s

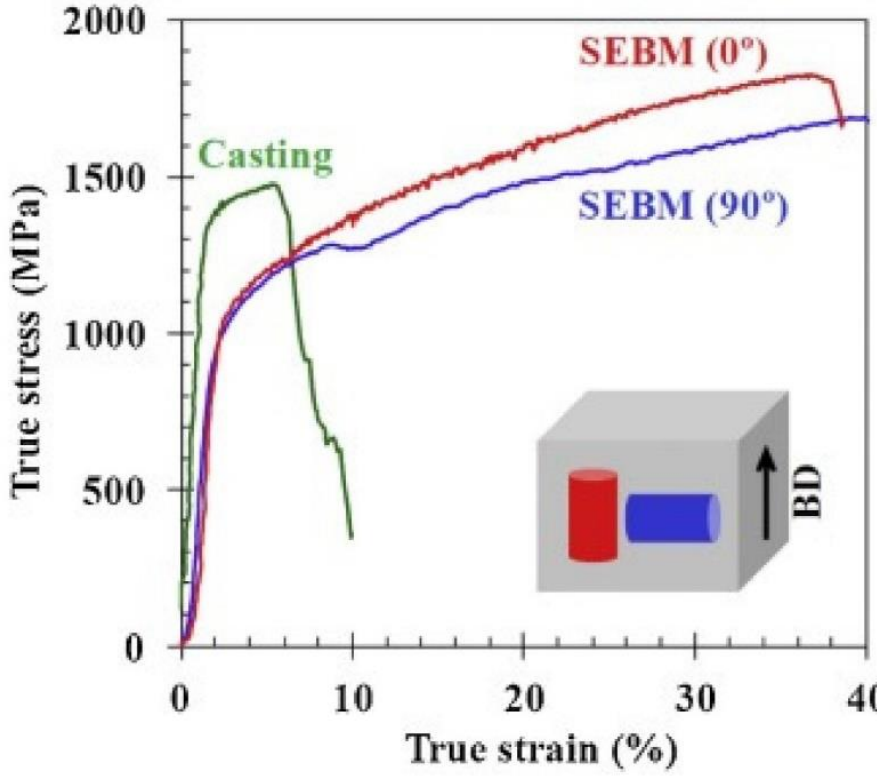

Fig. 5. True stress–strain plot of AlCoCrFeNi HEA fabricated using selective electron beam melting (EBM) and compared with as-cast sample [58].

.

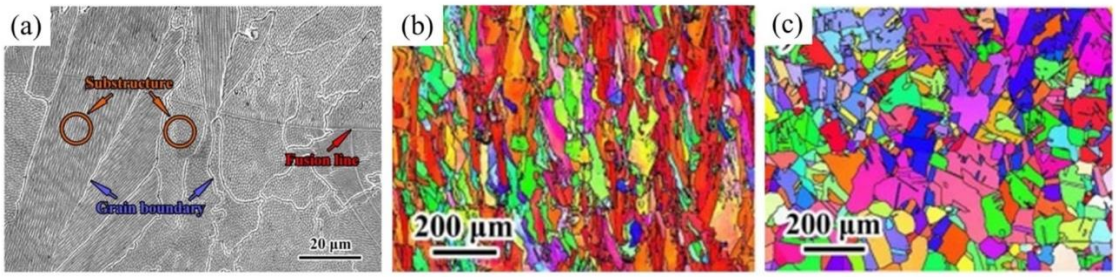

Fig 6. (a) SEM images of SLM-built CoCrFeNi HEA showing its cellular structure; EBSD of CoCrFeNi HEA in (b) as built and (c) annealed conditions, confirming columnar microstructure for as-built and equiaxed for annealed sample [64].

vier.

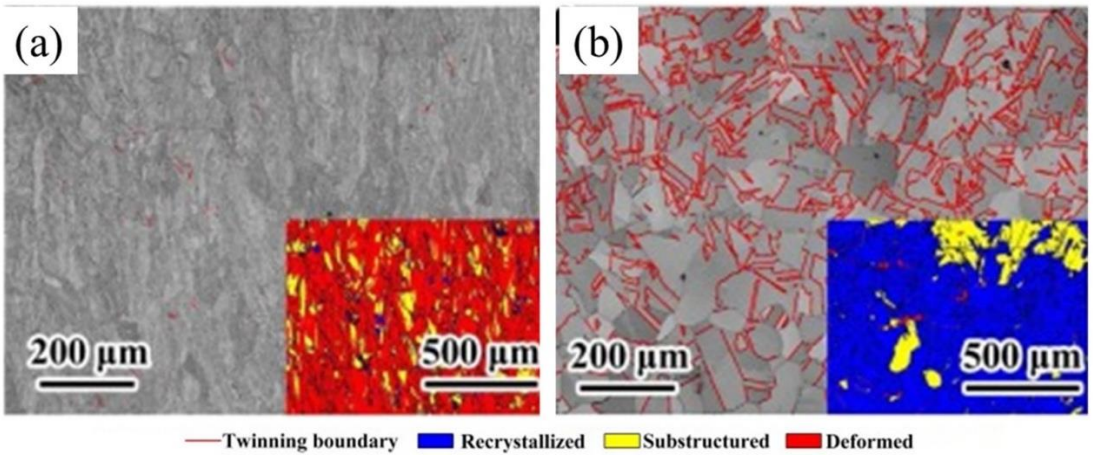

Fig. 7. Distribution of twinning for CoCrFeNi HEA in (a) as-built and (b) annealed at 1300 _C for 2 h conditions, indicating higher density of twinning after annealing. Insets show recrystallization di tribution map [64].

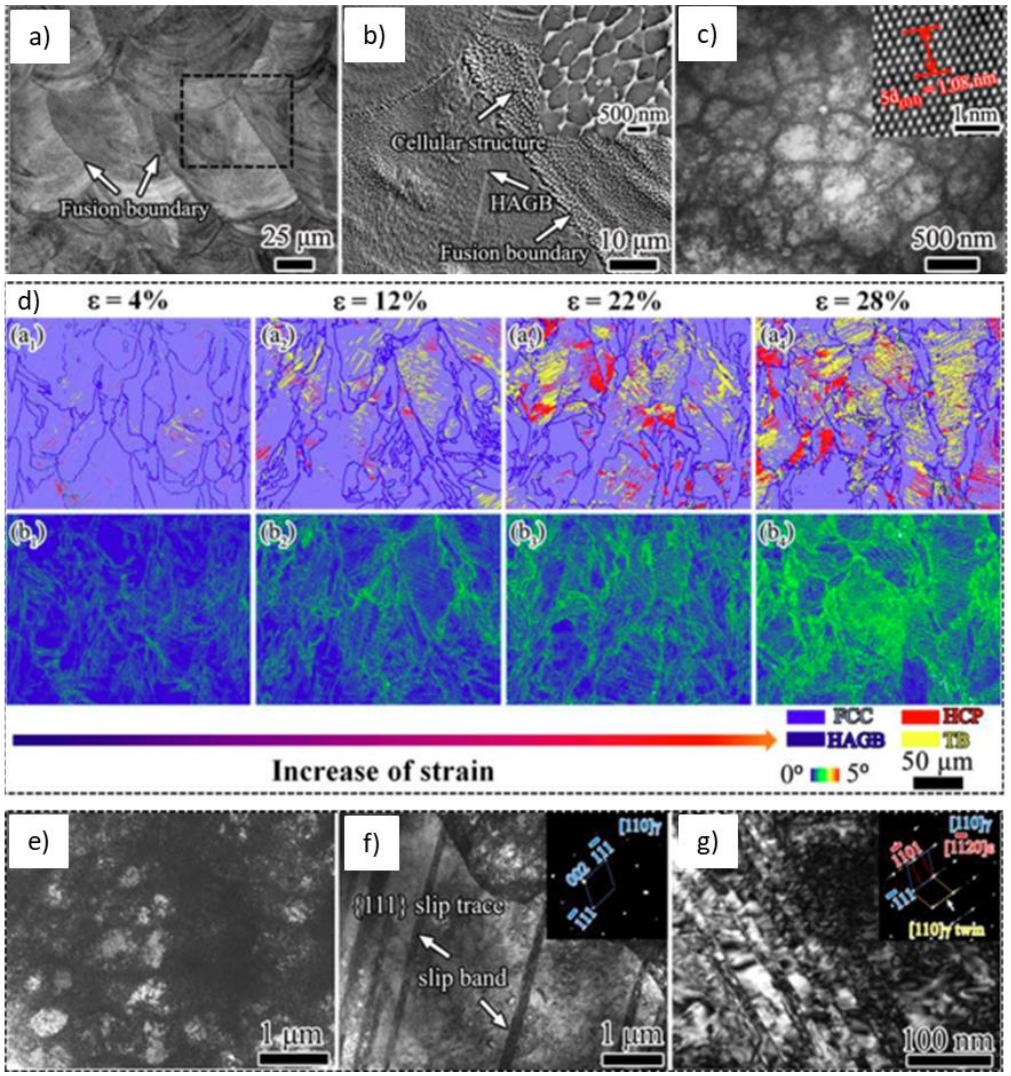

Fig. 8. (a) OM images of the as-built Fe49.5Mn30Co10Cr10C0.5 HEA. (b) SE image of dotted region in (a). The inset displays the equiaxed cellular structures. (c) STEM micrograph showing the equ axed cellular structures. The inset shows the distance across five {111} planes in HRTEM image. (d) (a1–a4) EBSD phase and GBs maps revealing microstructural evolution at different strain levels. TEM images of deformed structure for 4% strain (e, f) and 12%
strain (g). The insets show the SAED pattern [70]

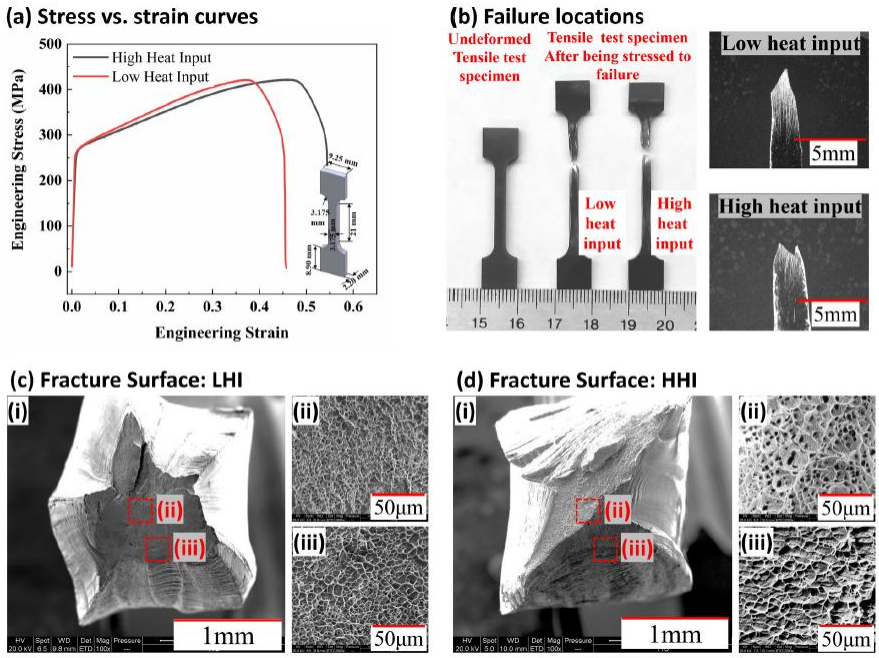

Fig. 9. (a) Stress vs. strain curves for the tensile testing of the deposits with two heat input conditions; (b) OM images showing the failure locations; and SEM images of the fracture surfaces of the (c) low heat input and (d) high heat input specimens [72].

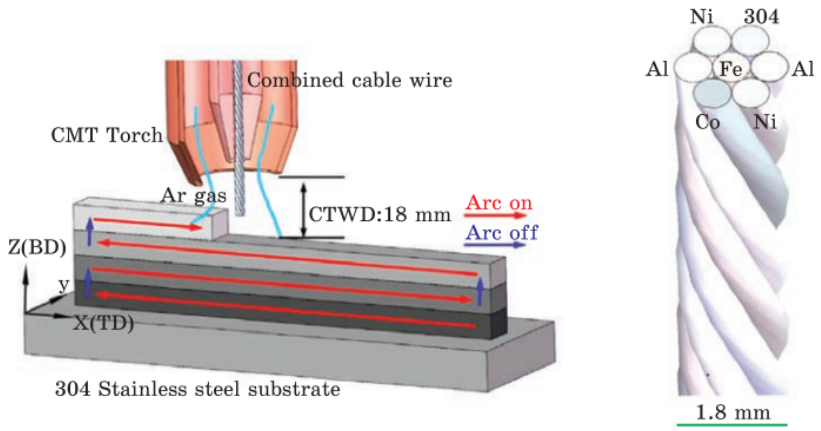

Fig. 10. (a) Schematic of the CCW-AAM technique used to create HEA and (b) 3D model of CCW [73] .

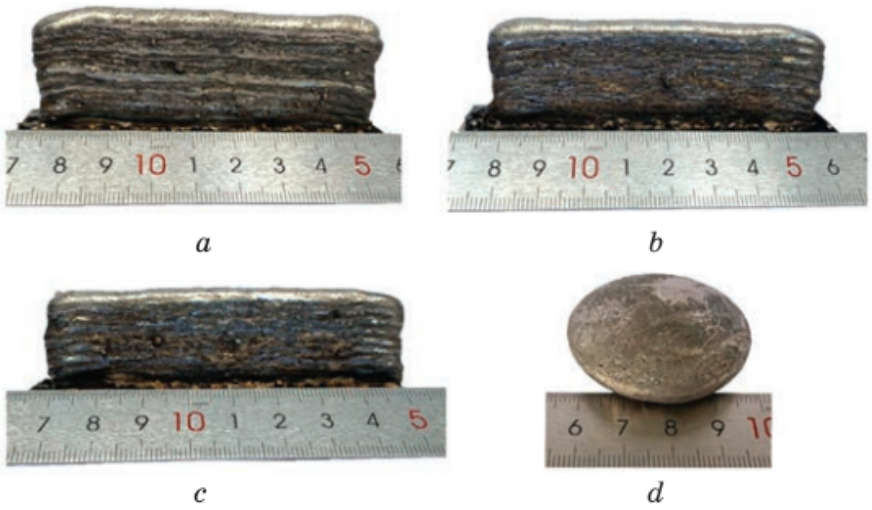

Fig. 11. Samples of Al-Co-Cr-Fe-Ni HEA fabricated using CCW-AAM: (a) 8 mm/s travel speed; (b) 10mm/s travel speed; (c) 12 mm/s travel speed; (d) vacuum arc casting [73].

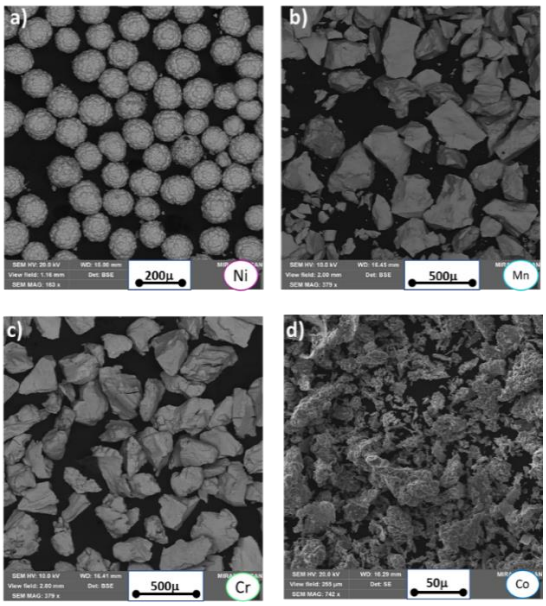

Fig.12. Metal powders used in wire manufacturing [74]

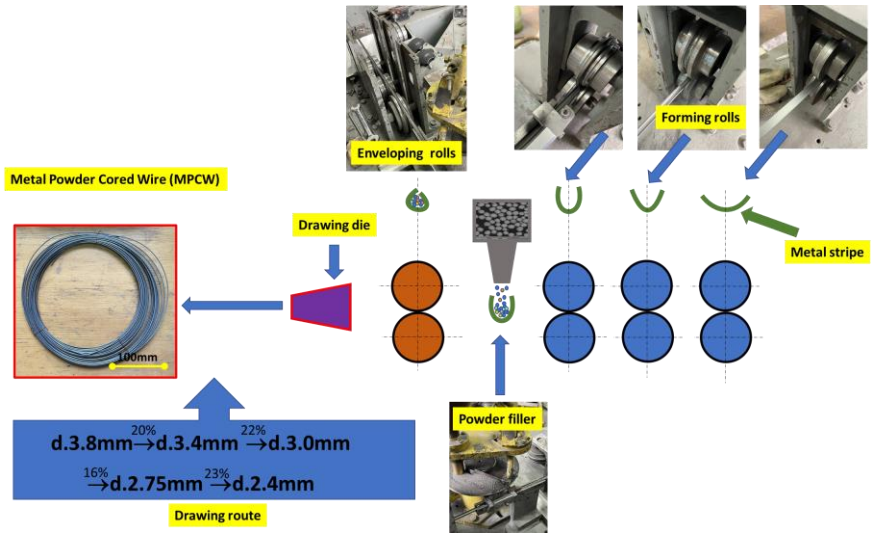

Fig. 13 - Scheme of the metal powder cored wire manufacturing

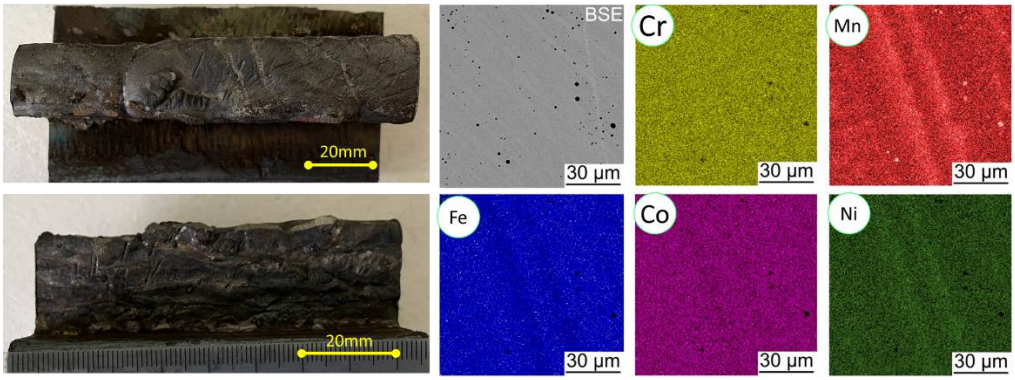

Fig. 14. A general view of deposits and a X-Ray maps of the chemical elements distribution

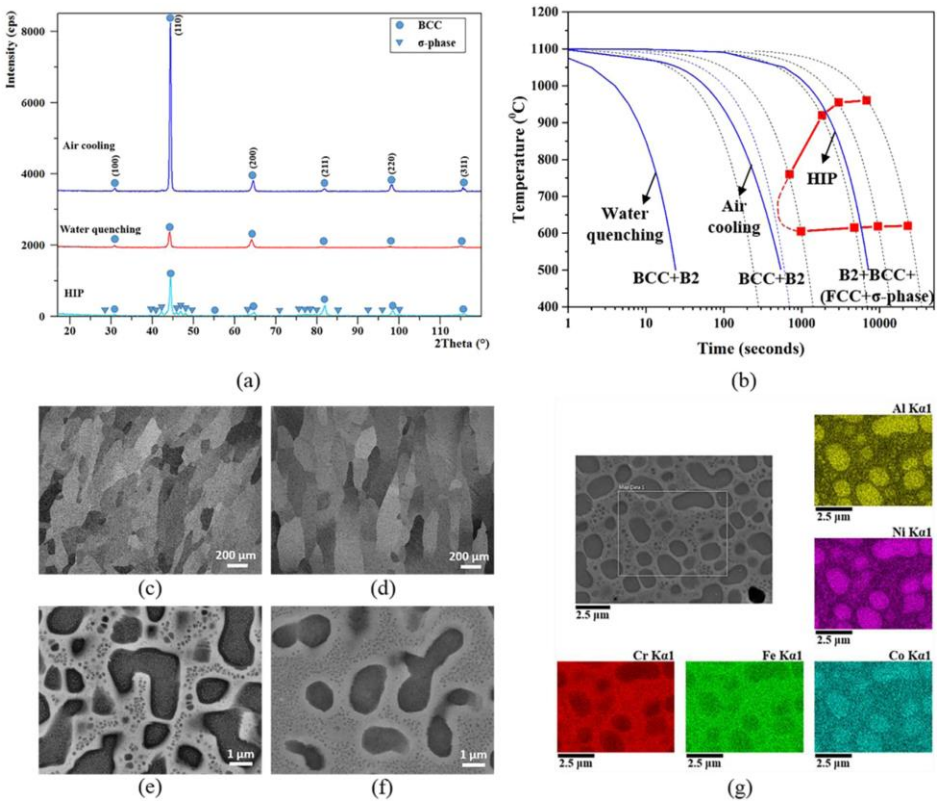

Fig. 15 (a) The XRD spectra of Al0.85CoCrFeNi HEA subjected to various post-processing heat treatments after solutionising at 1100 °C for 3 h with cooling rates of air-cooling water quenching and HIP (b) shown on the CCT curve of σ-phase in Al0.85CoCrFeNi alloy. SEM micrographs of Al0.85CoCrFeNi alloy solutionised at 1100 °C for 3 h followed by (c) air cooling and (d) water quenching and the corresponding micrographs at higher magnification is shown in (e) ,(f) and (g) respectively [92].